Title

CO(2) Electroreduction on Borated Copper Surfaces: Boron Active Sites, Not Copper

Journal

ACS Catalysis

ISSN

2155-5435

Authors

Goswami, Anubhav
Zhang, Zisheng
Alexandrova, Anastassia N

Publication Date

2026-05-26

DOI

10.1021/acscatal.6c02814

$CO_{(2)}$ Electroreduction on Borated Copper Surfaces: Boron Active Sites, not Copper

Anubhav Goswami,[1] Zisheng Zhang,[1,3] Anastassia N. Alexandrova,[1,2,*]

[1]Department of Chemistry and Biochemistry, [2]Department of Materials Science and Engineering, University of California, Los Angeles, USA, 90095

[3] SUNCAT Center for Interface Science and Catalysis, Department of Chemical Engineering, Stanford University, Stanford, California, USA, 94305

Corresponding Author's email: alexandrova@g.ucla.edu

Abstract

Boron-doped copper has recently emerged as an active and stable catalyst for the electrochemical reduction of CO_2 to value-added C_2 products. Here, we develop a realistic model of CO electroreduction on surface borides of copper under operational conditions, taking into account the effects of electrode potential, electrolyte environment, and pH. We study the possible reconstruction of the electrocatalyst surface using grand canonical DFT and global optimization to obtain a potential-dependent grand canonical ensemble description of metastable, hydrogen-covered catalyst surfaces. Two key surface configurations, low H-coverage (LC, -0.6 V_{SHE}) and high H-coverage (HC, -0.8 V_{SHE}) dominate this ensemble, with the former being kinetically persistent and C_2 selective under strongly reducing conditions. Nonmetallic boron sites on the surface copper boride are found to bind CO more strongly than copper sites, and mechanistic investigation of CO electroreduction pathways presents a surprisingly unconventional case of boron-centered reactivity in contrast to typical copper-centered reactivity. Neighboring boron sites present along boron chains on the surface copper boride are found to facilitate C–C coupling, thereby driving the high C_2 selectivity of this electrocatalyst.

Introduction

Electrocatalysis provides a sustainable platform for storage of renewable energy and the production of value-added chemicals.[1–4] Electrochemical reduction of CO_2 (eCO_2RR) is of added interest due to its potential toward closing the carbon cycle.[5,6] For eCO_2RR, Cu is the only transition metal to effectively convert CO_2 to valuable multi-carbon (C_{2+}) products such as ethylene and ethanol.[7,8] There have been multiple strategies to increase C_2 product selectivity and to tune the product distribution, including the design of multicomponent electrocatalysts by introducing metal hydroxides,[9,10] functionalizing electrodes with organic molecules to stabilize reaction intermediates,[11,12] and doping Cu with non-metals to promote Cu^+ states shown to be active for the C_2 production.[13–20] In particular, B-doped Cu has recently been shown by Sargent et al. to exhibit remarkable performance for the selective synthesis of C_2 products while remaining stable for prolonged durations.[21] Modelling $eCO_{(2)}RR$ on such surfaces has been performed in the past on a simplistic subsurface model, or embedded B-atoms on the Cu(100) or Cu(111) surfaces, without incorporating realistic reaction

conditions.[21,22] However, an accurate description of the electrocatalyst surface and accounting for its possible restructuring under operating conditions, by taking into consideration effects such as electrode potential, presence of electrolyte, and solution pH, is necessary to develop an understanding of these catalysts and their performance.

Here, we model eCORR (electrochemical CO reduction reaction) under realistic operational conditions, treating CO as an intermediate expected to be generated during CO_2RR and focus on its subsequent electroreduction on the reconstructed electrode surface. Without explicitly addressing the kinetics of site specificity of the preceding CO_2-to-CO step, including how rapidly CO forms or how it redistributes among available surface sites, we focus separately on the reconstruction of the electrode surface and mechanism of eCORR to probe the C_2:C_1 selectivity of the surface. The starting point is the previously experimentally characterized ordered surface borides of copper on Cu(111).[23–25] We constructed potential-dependent grand canonical ensemble and free energy landscape of the copper boride surface, to identify relevant coverage of *H at neutral pH and varying cathodic potentials. Both thermodynamic and kinetic considerations (accounting for reconstruction, dissolution, and hydrogen evolution reaction) are made to produce the relevant surface models, and to identify routes to potential surface degradation. At relevant cathodic potentials, CO adsorption showed a strong preference for B sites over Cu sites. Surprisingly, further mechanistic investigations revealed that B sites generally outperform Cu sites in CORR and are particularly superior for C–C coupling, leading to C_2 products. This work presents an unconventional instance wherein CORR chemistry occurs almost exclusively on B sites rather than Cu sites in contrast to typical non-metal doped Cu, and provides insights to develop an understanding of the activity, selectivity, and stability of this surface in catalyzing $eCO_{(2)}$RR. This will allow for the development of superior heterogeneous electrocatalysts for the efficient conversion of CO_2 to multi-carbon products.

Results and Discussion

Modelling electrocatalyst surface

We considered the ordered copper boride (referred to as CuB hereon) surface with stoichiometry Cu_8B_{14} which is reported to form after the deposition of boron on Cu(111) under ultrahigh vacuum. We constructed the unit cell consisting of a 4×1 supercell of CuB on a 3-layer $\sqrt{73} \times \sqrt{39}$ superstructure of Cu(111), as reported experimentally,[23] corresponding to a repeating $Cu_{32}B_{56}$ surface (Figure 1a). The pH, electric double layers, and electrode potential can cause substantial restructuring of the surface, and therefore, the configuration of the CuB surface under the coverage of H was subjected to global optimization using the grand canonical genetic algorithm (GCGA).[26–29] Notably, we sampled the positions of the Cu and B, and coverage of H atoms, to pursue possible reconstruction. The system was allowed to exchange H with a reservoir of hydrogen atoms held at a fixed chemical potential μ_{H} defined as:

$$\mu_{\mathrm{H}}(\mathrm{pH}, U, T) = \frac{1}{2}E_{\mathrm{H_2}}^{\mathrm{gas}} - \ln(10)\, k_{\mathrm{B}} T \mathrm{pH} - |e| U_{\mathrm{SHE}} + \left(\mathrm{ZPE}^{\mathrm{gas}} + C_p^{\mathrm{gas}} - \mathrm{TS}^{\mathrm{gas}}\right) - (\mathrm{ZPE}^{\mathrm{ads}} + C_p^{\mathrm{ads}} - TS^{\mathrm{ads}})$$

GCGA searches were carried out at the pH of 7 and multiple electrode potentials between 0 and -1.50 V_{SHE} to minimize the coverage-dependent grand canonical free energy Ω_{ads} defined as:

$$\Omega_{\mathrm{ads}} = U - TS - \mu_{\mathrm{H}} N_{\mathrm{H}} \approx E^{\mathrm{slab}-n_{\mathrm{H}}} - E^{\mathrm{slab}} - n_{\mathrm{H}}\mu_{\mathrm{H}}$$

In total, 4,191 unique structures for the CuB surface under H coverage were obtained. The results of grand canonical sampling at four cathodic potentials (-0.25 V_{SHE}, -0.50 V_{SHE}, -0.75 V_{SHE}, and -1.00 V_{SHE}) are illustrated in Figure 1 with H coverage represented by $\theta_H = n_H/n_B$. At -0.25 V_{SHE}, the process of H uptake by the CuB surface is initially thermodynamically unfavorable until around θ_H = 1.0, beyond which, further hydrogenation appears to be comparatively favorable but still overall endergonic. At more negative electrode potentials (Figure 1c-e), the H uptake becomes thermodynamically favorable compared to the bare surface without hydrogen. At -0.5 V (Figure 1c), a plateau of metastability appears, corresponding to a set of deep hydrides of the CuB surface. The hydrogenation occurs on the surface boron, in contrast to pure Cu surfaces that uptake H at cathodic potentials.[26–28] The preferential hydrogenation of B atoms over Cu atoms is likely due to stronger, covalent bonding in B–H compared to more ionic bonding in Cu–H. This is demonstrated by analyzing features of the charge density ρ using QTAIM (Quantum Theory of Atoms In Molecules).[30,31] Higher values of ρ (>0.1 a.u.) and generally negative values of $\nabla^2\rho$ (i.e. the Laplacian) at the B–H bond critical points are indicative of their covalent nature while the contrastingly lower values of ρ (<0.09 a.u.) and positive values of $\nabla^2\rho$ indicate ionic bonding in the Cu-H bonds (Figure S14). The sampling also shows that the thermodynamic global optimum corresponds to the uptake of even more H, with gradual breaking off of B atoms as borane-like structures, leading finally to the destruction of the B chains and likely borane dissolution. Besides borane formation, no substantial change of zigzag boron structures occurs, despite the sampling algorithm permitting it. Given the experimentally seen stability of the boron dopants on Cu in electroreduction conditions,[21] it appears that the degradation must be prevented by kinetic effects, i.e. substantial barriers to excess hydrogenation and/or B chain breaking (*vide infra*) and competing hydrogen evolution reaction (HER) which maintains intermediate H coverage on the surface. Indeed, under non-equilibrium conditions that persist in thermal and electrochemical conditions, it has been observed that relaxation of the system to the thermodynamic global minimum can exceed relevant reaction timescales.[26,28,32] For example, H coverage on Cu electrodes has been previously shown to be substantially lower than the thermodynamic prediction.[28] Along similar lines, we conjecture that the surface is trapped on the metastable hydride plateau (outlined in Figure 1c) during $CO_{(2)}$RR. Therefore, we constrained the upper limit of H coverage to ensure that the system has a maximum of one break-off B unit. Here, we only focus on the metastable H coverage regime outlined in Figure 1c (corresponding to GCGA sampling conducted at -0.5 V_{SHE}) and shown explicitly in Figure 1f, i.e., where θ_H ranges from 0.45 to 0.90 *(*corresponding to n_H = 25 to 50 per unit cell). This region exhibits a convex hull structure (Figure 1f), indicative of a local optimum in coverage. Note that for every θ_H, multiple possible structures are in a low energy window. A sub-ensemble is therefore constructed with configurations within 0.2 eV (corresponding to an equivalent Boltzmann population cutoff of 0.0005) of the global minimum at each coverage from the pool of configurations obtained from the GCGA sampling conducted at -0.5 V_{SHE}. This sub-ensemble covers the range where the B chains are majorly preserved on the surface due to kinetics, and only a minor breakage is observed.

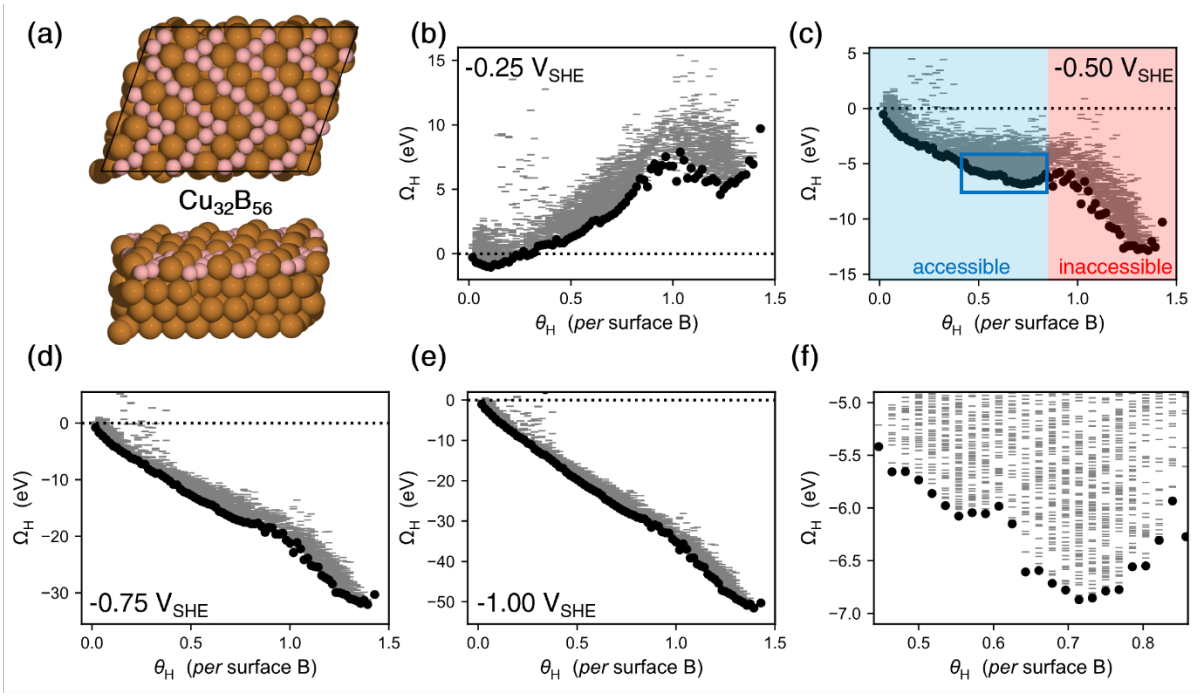

Figure 1. (a) $Cu_{32}B_{56}$/Cu(111) unit cell. (b)-(e) Grand canonical free energy as a function of H coverage (in terms of θ_H), at different electrochemical potentials (vs SHE); each dash corresponds to a unique sampled local minimum with the global minimum at each H coverage marked with a circle. The region shaded blue indicates the upper limit of H coverage adopted in this work, beyond which, in the region shaded red, the system is considered losing boron to the solution phase. The plateau of metastability in (c) is indicated with a blue box. (f) The metastable region at -0.5 V_{SHE} as marked in (c); this convex hull is observed with a local optimum at $\theta_H = 0.7$.

To assess the evolution of the surface H coverage under varying electrochemical potentials, we computed potential-dependent free energies for the states within the sub-ensemble via GCDFT (grand canonical DFT) and calculated their populations using Boltzmann statistics in the relevant potential regime (Figure 2). In the window of -0.5 V to -0.7 V_{SHE}, structures with lower H coverage (θ_H < 0.66) and limited B chain breaking dominate. Around the electrochemical potential of -0.7 V_{SHE}, this preference switches to higher H coverage (θ_H > 0.66) along with the initiation of B chain breaking. The configurations with higher H coverage include triply and quadruply hydrogenated B sites, with the latter being present as break-off units (Figure 2). In particular, configurations which showed a single B chain breaking were first found close to $n_H = 34$ per unit cell, or equivalently $\theta_H = 0.61$ (Figure S4), leading to a quadruply hydrogenated B site that exists as a break-off BH_4 unit (B-*out*). Subsequent hydrogenations of the doubly hydrogenated BH_2 unit (B-*in*) successively form a BH_3 unit (BH_2 + *H → BH_3) and then a BH_4 unit (BH_3 + *H → BH_4). Modelling this B-*in* to B-*out* transition and the competing HER on these BH_x sites hydogenation showed that B chain breaking associated with the excess hydrogenation of the B sites was found to have substantial kinetic barriers (Table 1) that are outcompeted by HER on these multiply hydrogenated B sites (see Supporting Information, Section S2 for more details), which likely precludes the complete hydrogenation of the surface B atoms and subsequent dissolution, providing additional support for our prior assumption of kinetic metastability of the surface (*vide supra*). The sharp switch to higher H coverage (Figure 2) is also likely to be restrained by these kinetic barriers to B chain breaking and as such, we anticipate the lower H coverage structures to dominate the catalyst ensemble at operational timescales. Similar kinetic stability of periodic surface B arrangements in the

hydride state has also been reported in the case of MoB_2.[33] The hydrogen-covered CuB surfaces were also found to be stable over 10 ps of unconstrained *ab initio* molecular dynamics (AIMD) simulations with explicit solvation, with no additional B chain breakage or B units floating into solution (see Supporting Information, Section S3). We note here that our model employs an implicit solvation treatment and does not account for any possible assistance by explicit solvent molecules in the B chain breaking via excess hydrogenation. Notwithstanding this limitation, the calculated barriers associated with B chain breaking are substantial, and the attainable H coverage on the surface is further limited by HER and $CO_{(2)}$RR pathways. Consequently, we expect our conclusions regarding the kinetic persistence of lower H coverage states to remain valid.

Table 1. Barriers (in eV) for B hydrogenation and Tafel HER transition states.

n_H	B hydrogenation		HER	
	$BH_2 + {}^*H \rightarrow BH_3$	$BH_3 + {}^*H \rightarrow BH_4$	$BH_2 \rightarrow B + H_2$	$BH_3 \rightarrow BH + H_2$
33	0.97	1.19	0.63	0.66
34	0.92	0.89	0.77	0.54

We found that within the region of potential importance in $CO_{(2)}$RR, i.e., -0.6 to -0.9 V_{SHE}, the structures with θ_H = 0.46 (n_H = 26 per unit cell) and θ_H = 0.70 (n_H = 39 per unit cell) have a particularly high (sometimes exclusive) population. Additionally, a single configuration corresponding to the global minimum (as shown in Figure 2) was found to contribute almost exclusively in case of both of the above coverages, i.e., for θ_H = 0.46 near -0.6 V_{SHE} and θ_H = 0.70 near -0.8 V_{SHE} (Figure S3). These configurations, hereafter referred to as low coverage, or LC (-0.6 V_{SHE}), and high-coverage, HC (-0.8 V_{SHE}), respectively (with the inclusion of the approximate potential at which each dominates the Boltzmann ensemble included in the nomenclature) were subjected to further investigation for their activity toward electrochemical CO reduction.

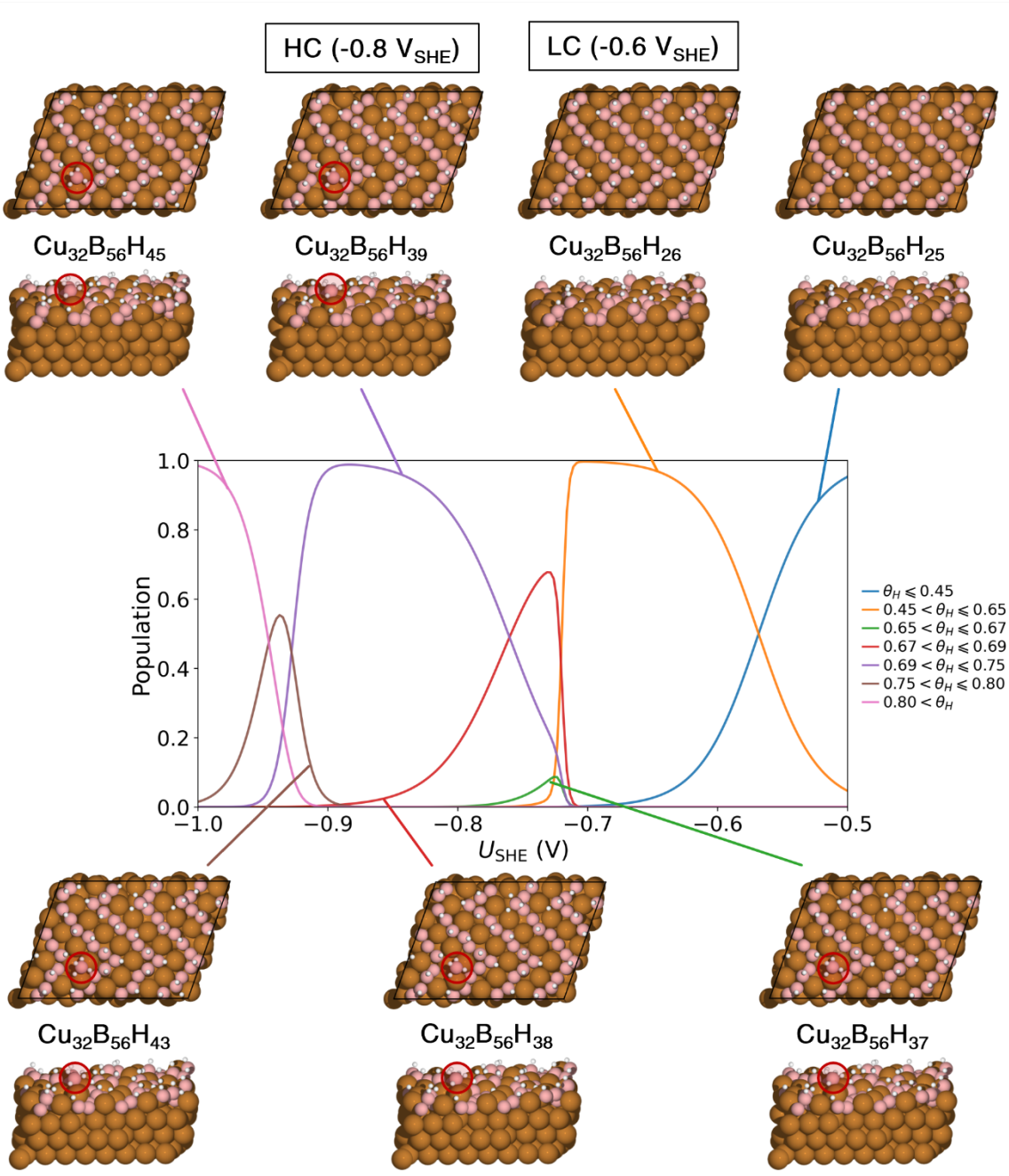

Figure 2. Boltzmann population of different H coverage ensembles as functions of electrochemical potential. The minimum energy structures (top and side views along with the stoichiometry of the corresponding unit cell) of each ensemble are shown, and break-off B units are circled in red. The predominant configurations LC (-0.6 V_{SHE}) and HC (-0.8 V_{SHE}) are denoted separately.

Bader charge analysis of the pristine and H-covered CuB (overall charge-neutral) surface was carried out to understand the influence of H coverage on the electronic structure of the surface (Figure 3). For the pristine surface, the surface B and Cu atoms carry an average Bader charge of -0.24 *e* and +0.29 *e* respectively, indicating oxidation of the surface Cu by the B atoms. Specifically, among the B atoms, those at the corners of the zigzag B chains are least negatively charged and become progressively more negatively charged toward the center of the zigzag chains.[23,24] The B atoms covered with H atoms, having transferred electron density

to the respective H atoms, are positively charged. Among the B atoms without B-H bonds, the extent of negative charge is seen to follow the geometric trend observed for the pristine surface. Therefore, the final charge of a surface B atom depends on both the presence or absence of H atoms bound to it and its location in the B chain, i.e., a combination of charge transfer to and from coordinating H and Cu atoms on the surface. On a separate note, the potential of zero charge (PZC) on the H-covered CuB surface is calculated to be 0.18 V for the low H-coverage state LC (-0.6 V_{SHE}) and 0.08 V for the high H-coverage state HC (-0.8 V_{SHE}) – substantially more positive than that of pure Cu (~-0.5 V_{SHE}).[34–36] Thus, in the potential regime of interest, the CuB surface operates much further below its PZC and carries a significantly higher negative surface free charge compared to Cu electrodes. This hints toward an enhanced electrostatic accumulation of electrolyte cations in the interfacial region, particularly in proximity to the B sites, resulting in stronger interfacial electric field near the B sites in CuB compared to pure Cu.

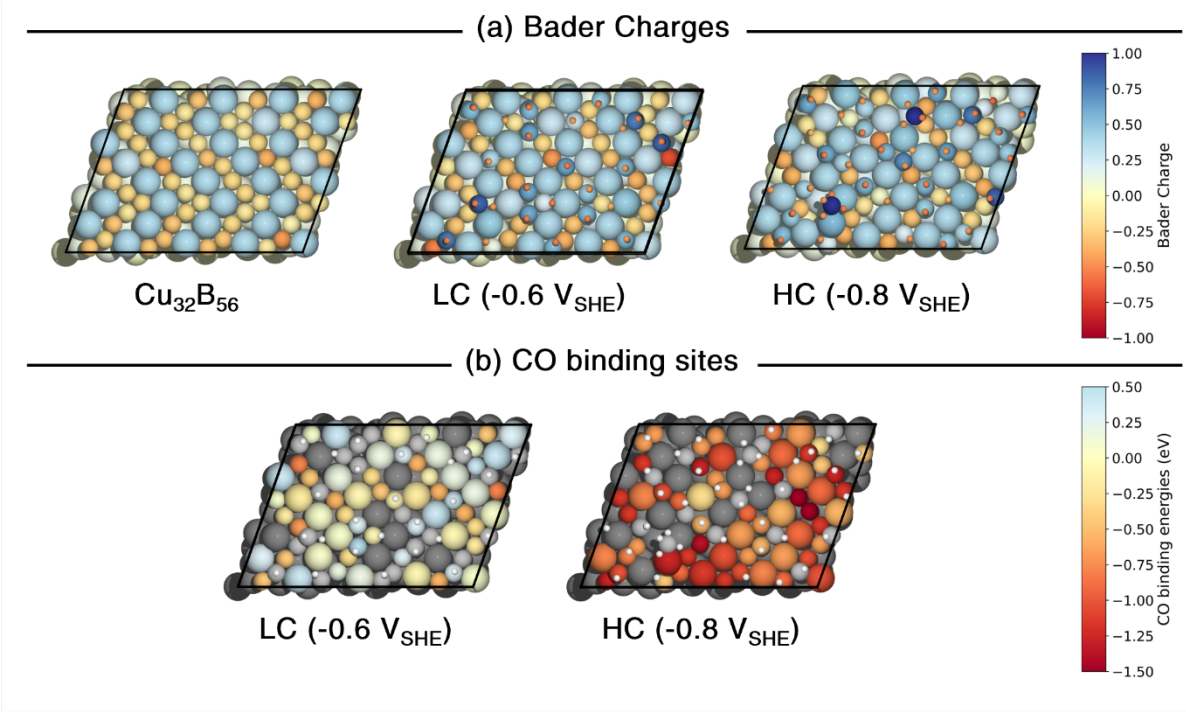

Figure 3. (a) Bader charges of the pristine and H-covered CuB surface configurations LC (-0.6 V_{SHE}) and HC (-0.8 V_{SHE}) which dominate the Boltzmann ensemble at -0.6 V_{SHE} and -0.8 V_{SHE} respectively. (b) Site-dependent CO binding energies on the predominant H-covered CuB surface configurations. Note that sites where CO did not bind successfully are colored dark grey and light grey for Cu and B respectively.

To identify potential sites for CORR, we sampled CO binding at different sites on the hydrogenated CuB surface. The large size of the unit cell made an extensive GCGA sampling of CO (in addition to surface restructuring and H coverage) prohibitively expensive, and we therefore resorted to a combination of one-shot sampling methods implemented in GOCIA[29] for CO adsorption (see Supporting Information, Note 2). The CO binding sites thus obtained are visualized in Figure 3b with their associated binding energies. The strongest CO binding corresponds to a binding energy ($\Delta E_{b,CO}$) of -0.76 eV (corresponding binding free energy, $\Delta G_{b,CO}$ = -0.22 eV) at LC (-0.6 V_{SHE}) and -1.49 eV ($\Delta G_{b,CO}$ = -0.82 eV) at HC (-0.8 V_{SHE}). It was observed that, in general, CO preferentially binds to the B atoms rather than the Cu atoms on

the surface at both LC (-0.6 V_{SHE}) and HC (-0.8 V_{SHE}). We attribute this to the higher electron density on the B atoms relative to Cu, which leads to enhanced electrostatic attraction for the protons arriving from solution, and stronger boron-to-ligand π-backbonding, therefore strengthening the B-CO bond compared to the Cu-CO bond (see Supporting Information, Section S5). In some cases, CO binds to H-covered B sites by displacing the adsorbed *H to a neighboring site; however, these instances do not correspond to the strongest CO binding (Figure 3b). Most of the other B sites capable of binding CO strongly generally fall into one of two categories, being part of either a B_{3+} chain, i.e., three or more consecutive B atoms without H atoms, or part of a B_2 chain, i.e., two consecutive B atoms without H atoms. This categorization is anticipated to be useful later in the context of C_2 reaction pathways since C–C coupling on B sites in a B_2 chain necessitates CO adsorption on neighboring B atoms whereas on B sites in a B_{3+} chain, it may proceed from CO adsorption on alternate B atoms. We consider a number of these CO binding sites (both B and Cu) for subsequent mechanistic investigation at each of the above electrochemical conditions.

Mechanistic study of C_1 and C_2 pathways

Achieving a high C_2 vs C_1 selectivity during eCORR is of fundamentally high importance, and B-doped Cu has been reported to be highly selective for the formation of C_2 products.[21] To this end, we carried out mechanistic studies of C_1 and C_2 pathways on the CuB surface under applied electrochemical potential and the appropriate surface H coverage. Previous mechanistic studies modelling CO reduction on Cu have identified key steps and intermediates leading ultimately to C_1 and C_2 products (Scheme 1).[37–41] For C_1 products, this involves the hydrogenation of CO to CHO or COH and their subsequent hydrogenation to CHOH, which ultimately leads to C_1 products. For C_2 products, the reaction proceeds via the C-C coupling of neighboring CO molecules to produce CO–CO, or of CO with a hydrogenated intermediate to produce CO–COH or CO–CHO. These are the reaction intermediates we modelled on the different B and Cu sites as discussed above.

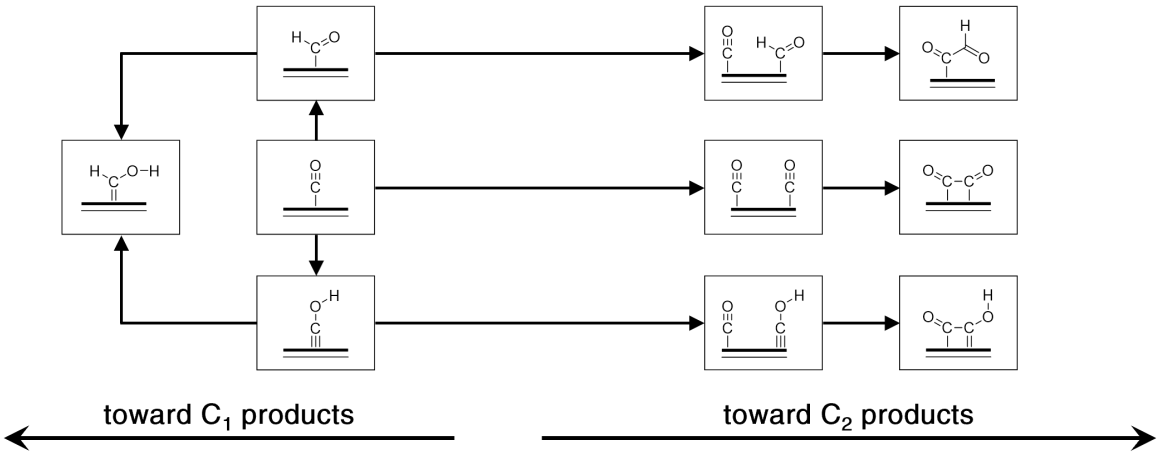

Scheme 1. CORR pathways toward C_1 and C_2 products.

The reaction intermediates for the C_1 and C_2 pathways were modelled on various CO binding sites at LC (-0.6 V_{SHE}) and HC (-0.8 V_{SHE}) (Figure 4). To keep the problem tractable, we used a $\Delta G_{b,CO}$ cutoff of 0.6 eV (compared to the strongest CO binding site) when considering various sites for this mechanistic investigation. This results in 20 and 22 different sites respectively in

the two electrochemical conditions, as highlighted in Figure 4a,d. At LC (-0.6 V_{SHE}), all the sites satisfying this cutoff at B sites and we therefore took the strongest CO binding Cu site (marked as site 4 in Figure 4a) additionally into consideration, to be comprehensive. For each reaction intermediate, a spectrum of site-dependent free energies is observed, of which, the site corresponding to the minimum free energy is highlighted and numbered in Figure 4a,d.

The ensemble-averaged reaction free energy for each process, $\langle \Delta G_{rxn} \rangle$, is thus obtained by Boltzmann-weighting the ΔG_{rxn} values, using $\Delta G_{b,CO}$ at that site as a weighting factor:

$$\langle \Delta G_{\mathrm{rxn}} \rangle = \frac{\sum_i \Delta G^i_{\mathrm{rxn}} \exp\left(-\frac{\Delta G^i_{\mathrm{b,CO}}}{k_B T}\right)}{\sum_i \exp\left(-\frac{\Delta G^i_{\mathrm{b,CO}}}{k_B T}\right)}$$

This ensemble-averaging is intended to provide an effective thermodynamic descriptor of the accessible ensemble of CO binding sites, rather than a direct kinetic measure of catalytic activity. This approximation therefore emphasizes strongly binding sites and does not explicitly account for site-dependent activation barriers. Consequently, using the Brønsted-Evans-Polanyi (BEP) principle directly here could cause the ordering of reaction free energies and activation barriers to differ, particularly if the relationships differ between competing steps such as CHO formation and CO dimerization. Accordingly, the ensemble-averaged reaction free energies are used only to compare the thermodynamic accessibility of intermediates across the site ensemble, while kinetic selectivity is assessed separately using explicit barrier calculations (*vide infra*). The application of Boltzmann weighting here should not be interpreted as assuming full equilibration of the entire catalyst surface, but rather as a quasi-equilibrium approximation for CO occupation across accessible sites within a given metastable surface configuration. The resulting $\langle \Delta G_{rxn} \rangle$ values are therefore best viewed as population-weighted effective reaction free energies for the selected ensemble of CO-covered sites, rather than outputs of a complete microkinetic model.

For the C_1 pathway, *CO hydrogenation to *CHO is more favorable than *CO hydrogenation to *COH, which demands a significantly higher free energy penalty, at both conditions. Specifically, $\langle \Delta G_{rxn} \rangle$ *CHO formation has values of +0.08 eV at LC (-0.6 V_{SHE}) and +0.01 eV at HC (-0.8 V_{SHE}). The corresponding values for *COH formation are +1.68 eV at LC (-0.6 V_{SHE}) and +1.46 eV at HC (-0.8 V_{SHE}) – this stark destabilization of *COH intermediates appears to be due to the linear chain-like nature of the surface B and Cu atoms which do not coordinatively saturate the *COH fragment (Figure 4g), analogous to a “top” site on Cu(111). Indeed, in the case of the most stable *COH binding state in HC (-0.8 V_{SHE}) labelled in Figure 4e, which is also the only *COH state within 0.5 eV of the most stable *CHO state, involves a B chain breakage, creating a “hollow” site in order to coordinatively saturate the *COH fragment (Figure S15) – the energetic cost of B chain breakage, nevertheless, renders the *COH state non-competitive in the electroreduction pathways. Both *CHO and *COH states are significantly destabilized at the Cu sites compared to the B sites. Relative to the lowest energy configuration, the most stable Cu-bound *CHO state is destabilized by +0.94 eV at LC (-0.6 V_{SHE}) and +0.62 eV at - HC (-0.8 V_{SHE}). The corresponding destabilization of the most stable Cu-bound *COH state is 1.51 eV at LC (-0.6 V_{SHE}) and 1.36 eV at HC (-0.8 V_{SHE}). Thus, *CHO formation is more favorable at the more cathodic potential and higher H-coverage and thermodynamically more facile at the B sites than the Cu sites. Sequential hydrogenation from *CO to *CHOH has $\langle \Delta G_{rxn} \rangle$ values of 0.13 eV at LC (-0.6 V_{SHE}) and 0.31 eV at HC (-0.8 V_{SHE}).

We calculated free energy barriers for *CHO formation at various sites to estimate the kinetics for entering the C_1 pathway. A spread in *CHO formation barriers is observed and Boltzmann-weighting them by the site-specific $\Delta G_{b,CO}$ gives an ensemble-averaged free energy barrier of 0.93 eV at LC (-0.6 V_{SHE}) and 0.78 eV at HC (-0.8 V_{SHE}). Note that in all steps modelled here, the proton originates from a hydrogen atom bonded to the surface, thus conserving n_H at each reaction step for a given configuration, and allowing direct comparison of GCDFT-derived energies at respective constant electrode potentials.

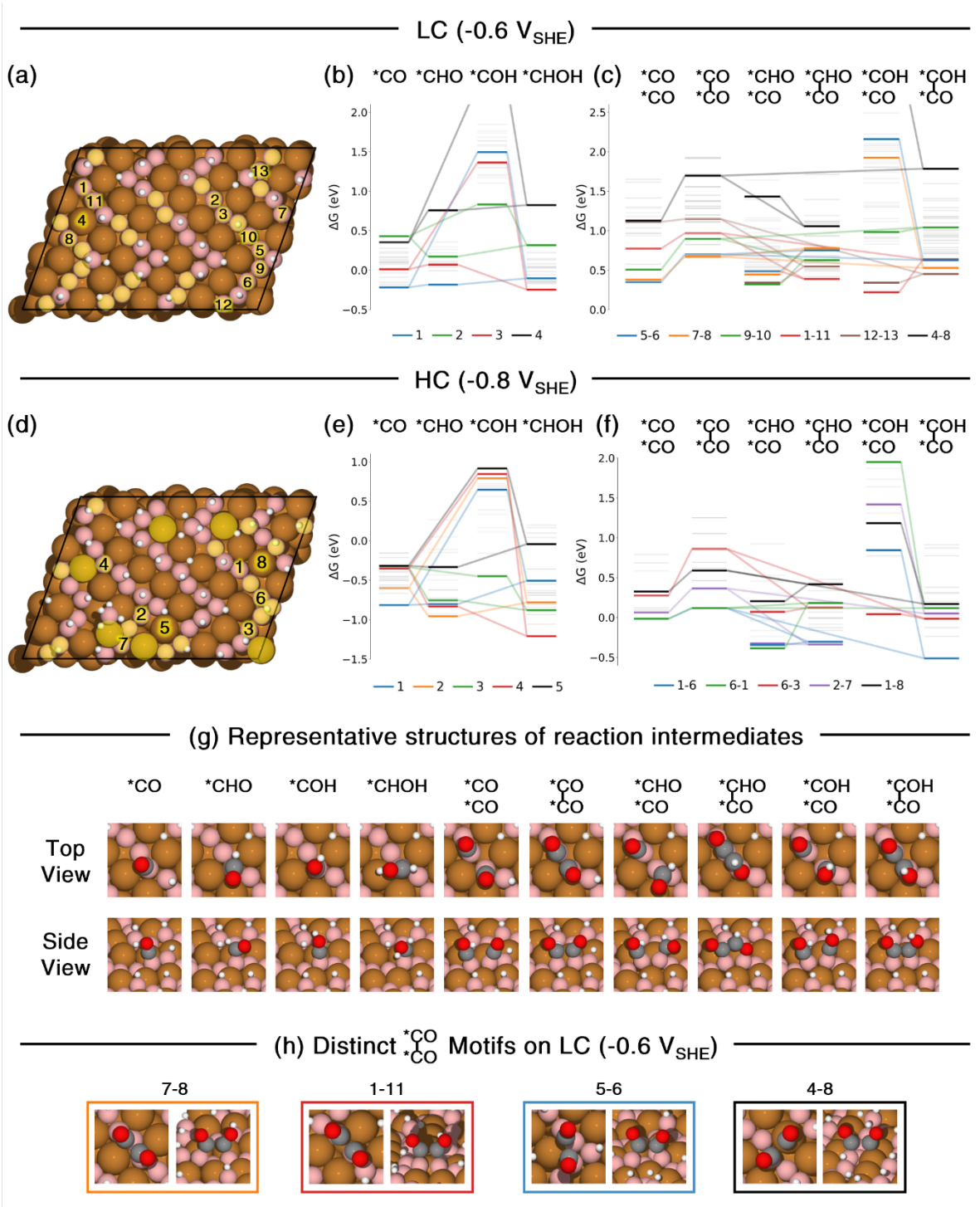

Figure 4. B and Cu sites considered for CORR on predominant H-covered CuB surface configurations (a) LC (-0.6 V_{SHE}) and (d) HC (-0.8 V_{SHE}). Note that the site labels in (a) and (d)

correspond to different sites. Gibbs free energy profiles for reaction pathways leading to (b), (e) C_1 and (c,f) C_2 products at LC (-0.6 V_{SHE}) and HC (-0.8 V_{SHE}), respectively. Gibbs free energies are calculated relative to the respective H-covered CuB surface. For each intermediate, the site corresponding to the minimum free energy is highlighted in color and labelled, and all the intermediate states at such sites are connected in the profile. States corresponding to intermediates at all other sites are colored light grey for clarity. (g) CORR reaction intermediate structures on site 3 at LC (-0.6 V_{SHE}). (h) $*C_2O_2$ motifs on distinct sites at LC (-0.6 V_{SHE}) including B_3 (7-8, 5-6), B_2 (1-11), and Cu-B (4-8) sites.

For the C_2 pathway, routes via *CO dimerization, and C–C coupling to form *CO–COH and *CO–CHO were considered. Notably, none of the C–C coupled species were stable on neighboring Cu sites and promptly dissociated upon relaxation. Therefore, we only considered neighboring B sites, and neighboring B and Cu sites, for C_2 pathways. Due to the high destabilization of the initial state containing *COH species relative to *CO and *CHO species, the *CO–COH pathway for the formation of C_2 product is ruled out on all of the considered sites. Both the CO dimerization and the *CO–CHO coupling pathways are probable based on the free energies of their corresponding intermediates. Specifically, the $\langle \Delta G_{\mathrm{rxn}} \rangle$ for CO dimerization is 0.34 eV at LC (-0.6 V_{SHE}) and 0.15 eV at HC (-0.8 V_{SHE}) when ensemble-averaged across all considered sites. The corresponding value of ΔG_{rxn} on the neighboring Cu–B sites at LC (-0.6 V_{SHE}) (4-8 in Figure 4c) is 0.56 eV, largest among all sites. At HC (-0.8 V_{SHE}), CO dimerization is comparatively more facile at Cu–B site (1-8 in Figure 4f), with a ΔG_{rxn} of 0.26 eV. *CO–CHO formation has a $\langle \Delta G_{\mathrm{rxn}} \rangle$ equal to 0.31 eV and 0.39 eV at LC (-0.6 V_{SHE}) and HC (-0.8 V_{SHE}) respectively. Since *CO–CHO formation through this route must necessarily be preceded by *CHO formation, and the latter's conversion to *CHOH formation is thermodynamically more favorable, we also discard the C–C coupling process for *CO–CHO formation in favor of CO dimerization as an entry point into the C_2 pathway. Free energy barriers for CO dimerization calculated at various sites have an ensemble-average value of 0.55 eV at LC (-0.6 V_{SHE}) and 0.44 eV at HC (-0.8 V_{SHE}).

The configuration for CO dimerization, involving two *CO molecules on nearby sites, incurs a thermodynamic penalty relative to the one *CO configurations. Thus, it may not be appropriate to compare the intrinsic free energy barriers for the *CHO formation and CO dimerization processes directly, since they are referenced to different initial states. We therefore compare Gibbs free energies of the transition states ($\Delta G^{\ddagger}$) for CO dimerization and *CHO formation directly and quantify C_2/C_1 selectivity using $\Delta\Delta G^{\ddagger}$(CO dimerization – *CHO formation) (Figure 5). As noted previously, we expect the lower H coverage state, represented by the LC (-0.6 V_{SHE}) state, to dominate the catalyst ensemble at operational timescales due to kinetics associated with excess hydrogenation and B chain breaking, even at lower electrode potentials at which HC (-0.8 V_{SHE}) is thermodynamically more stable. We therefore calculate the C_2/C_1 selectivity at the LC (-0.6 V_{SHE}) state (and at the HC (-0.8 V_{SHE}) state, for comparison) as a function of the varying electrode potential. While C_1 and C_2 processes appear evenly matched for the LC (-0.6 V_{SHE}) state of the catalyst near -0.5 V_{SHE}, the calculated C_2:C_1 distribution indicates increasing C_2 selectivity as the electrode potential is further lowered, with complete C_2 selectivity near -1.5 V_{SHE}. This is qualitatively similar to the selectivity switch observed by Sargent et al. in the case of B-doped Cu.[21] In contrast, the HC (-0.8 V_{SHE}) state of the catalyst shows complete C_1 selectivity across the potential range considered here. Thus, the kinetically metastable LC (-0.6 V_{SHE}) state of the catalyst endows it with high C_2 selectivity at electrode potentials below -0.6 V_{SHE}. The transition to the thermodynamically more stable

HC (-0.8 V_{SHE}) is kinetically hindered and would likely abolish C_2 selectivity while promoting C_1 product formation, contrary to experimental observations – unless other C_2 pathways not considered here prevail.

HER is generally an unavoidable side-reaction in aqueous electrocatalysis,[6,21,26,27,39] competing with $eCO_{(2)}RR$, particularly when sharing similar onset potentials. We therefore inspected the tendencies of the predominant H-covered CuB surfaces LC (-0.6 V_{SHE}) and HC (-0.8 V_{SHE}) to undergo HER. We considered both the Tafel and Volmer-Heyrovsky mechanisms at these configurations. The Tafel barriers (two *H coupling involving the least strongly bound *H) for the preferred configurations at LC (-0.6 V_{SHE}) (with n_H = 26 per unit cell) and HC (-0.8 V_{SHE}) (with n_H = 39 per unit cell) were calculated to be 0.52 eV and 0.26 eV respectively. The Volmer-Heyrovsky mechanism involves the initial Volmer step ($*H_n + H^+ + e^- \rightarrow *H_{n+1}$) and the subsequent Heyrovsky step ($*H_{n+1} + H^+ + e^- \rightarrow *H_n + H_2$) resulting in hydrogen evolution. We calculated the ΔG_{rxn} for each step starting from the aforementioned global minimum configurations with implicit solvation. At LC (-0.6 V_{SHE}), the relevant process was $*H_{26} \rightarrow *H_{27} \rightarrow *H_{26}$, where the ΔG_{rxn} for the Volmer and Heyrovsky steps were +0.20 eV and -0.14 eV respectively. At HC (-0.8 V_{SHE}), the relevant process was $*H_{39} \rightarrow *H_{40} \rightarrow *H_{39}$, where the Volmer and Heyrovsky steps involved ΔG_{rxn} of +0.26 eV and -0.60 eV respectively. Clearly, in both cases the penalty for HER originates from the initial change in configuration starting from a global minimum structure. Volmer-Heyrovsky steps may also be initiated from closely related structures, which can be accessible during operational conditions while involving the global minimum structure as an intermediate state. At LC (-0.6 V_{SHE}), considering the process originating from a $*H_{25}$ state (+0.04 eV above the global minimum $*H_{26}$), $*H_{25} \rightarrow *H_{26} \rightarrow *H_{25}$, we find that the Volmer and Heyrovsky steps have ΔG_{rxn} of -0.04 eV and +0.10 eV respectively. The case is slightly different at HC (-0.8 V_{SHE}), where the process originating from a $*H_{38}$ state (+0.04 eV above the global minimum $*H_{39}$), $*H_{38} \rightarrow *H_{39} \rightarrow *H_{38}$, has both the Volmer and Heyrovsky steps being thermodynamically favorable with ΔG_{rxn} equal to -0.04 eV and -0.29 eV respectively. Other states with potentially more favorable HER thermodynamics may participate in HER but are likely to not be prominent owing to their relatively miniscule populations. In summary, we find HER to be an unavoidable and competing process parallel to $CO_{(2)}RR$, as also observed by Sargent and co-workers in the case of B-doped Cu.[21] Additionally, persistent HER on the surface likely plays a role in maintaining the intermediate H coverage, preventing the system from reaching very high H coverage, and thereby preserving the B chains on the surface. For a more quantitative connection to the CO dimerization process, a direct comparison of the barrier for the Tafel HER process and the most feasible CO dimerization on the C_2 selective configuration LC (-0.6 V_{SHE}) was made. At -0.6 V_{SHE} (where the configuration is not yet C_2:C_1 is close to 1), the $\Delta\Delta G^{\ddagger}$(CO dimerization – HER) was calculated to be -0.09 eV indicating competitive HER. At the totally C_2-selective potential of -1.5 V_{SHE}, however, $\Delta\Delta G^{\ddagger}$(CO dimerization – HER) is equal to -0.34 eV, implying that CO dimerization outcompetes the HER.

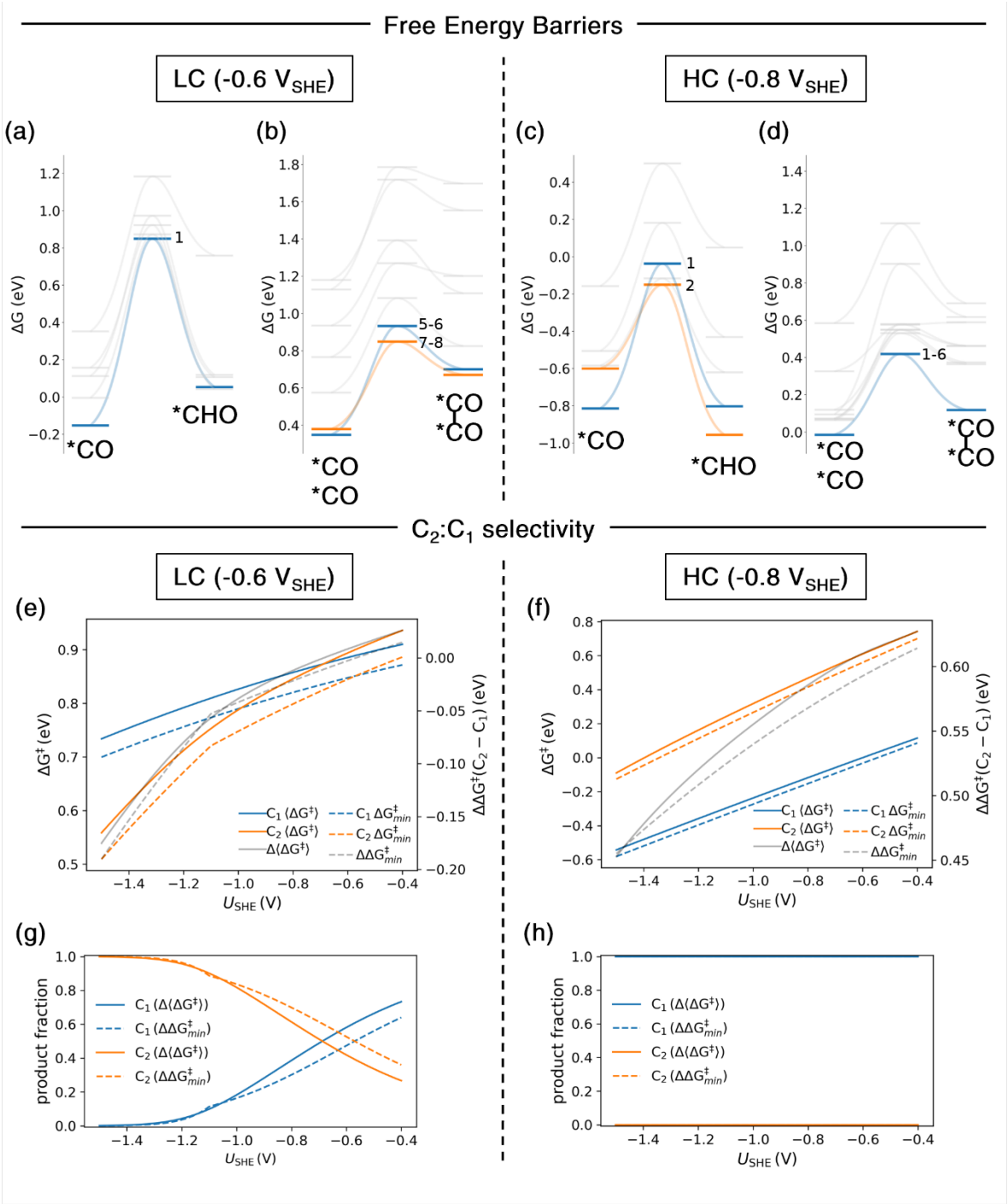

Figure 5. Free energy barriers for (a) *CHO formation and (b) CO dimerization at LC (-0.6 V_{SHE}); (c) *CHO formation and (d) CO dimerization HC (-0.8 V_{SHE}). Only the sites with the lowest energy transition state, initial state, or final state are colored and labeled; the coloring and labeling schemes from corresponding pathways in Figure 4 are maintained here. Minimum and ensemble-averaged $\Delta G^{\ddagger}$ for entering C_1 and C_2 pathways and their difference ($\Delta\Delta G^{\ddagger}$) at (e) LC (-0.6 V_{SHE}) and (f) HC (-0.8 V_{SHE}) as a function of electrode potential. C_1 and C_2 product distribution calculated for (e) LC (-0.6 V_{SHE}) and (f) HC (-0.8 V_{SHE}) as a function of electrode potential. All Gibbs free energies are calculated relative to the respective H-covered CuB surface.

A closer look at configurations with most facile CO dimerization (Figure 6a) reveals that each of them involves CO adsorption on alternate B atoms in B_{3+} chains whereas other configurations involve CO adsorption on adjacent B atoms, either in B_2 or B_{3+} chains, prior to coupling. To gain further insight into the higher C_2 activity of configurations with CO adsorbed on alternate sites in B_{3+} chains relative to those adsorbed on B_2 chains, we performed crystal orbital Hamilton population (COHP) analysis[42] of the fragments involving the respective B sites and CO molecules in the reactant and product states of CO dimerization. The obtained COHP is integrated up to the Fermi level to yield negative integrated COHP ($-\mathrm{ICOHP}_{E_F}$), which acts as a descriptor of the strength of the covalent and noncovalent interactions. In line with the positive ΔG_{rxn} for CO dimerization, a decrease in the magnitude of $-\mathrm{ICOHP}_{E_F}$ along the reaction coordinate was observed. It was noted that, for the B_3 site (i.e., three consecutive B atoms on a B_{3+} chain) under consideration, the change of magnitude of $-\mathrm{ICOHP}_{E_F}$ was much lower compared to the B_2 sites (i.e., two consecutive B atoms on a B_2 chain) – likely arising from the lower extent of distortion and strain in the fragment upon CO dimerization to form a five-membered ring at a B_3 site versus a four-membered ring at a B_2 site (Figure 6). This provides an indication as to why CO dimerization is easier at the B_3 site. Additionally, inspection of Bader charges for these configurations showed that the electronics associated by facile CO dimerization is primarily attributed to the B sites rather than the adjacent Cu atoms (Table S4).

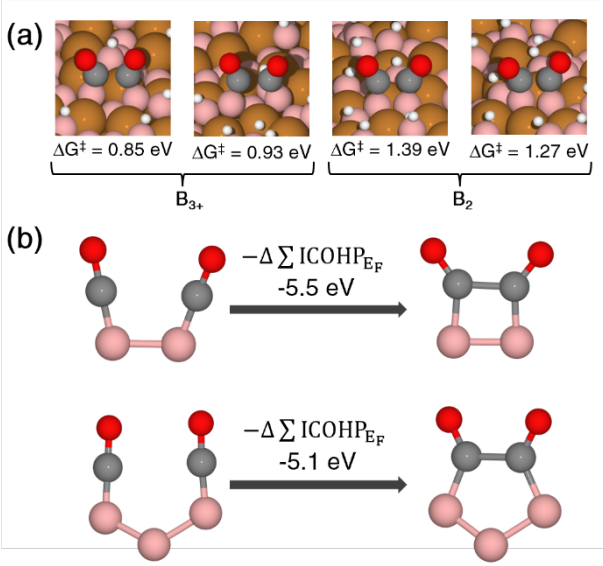

Figure 6. (a) Lowest energy CO dimerization transition states on B_2 and B_{3+} chains and their corresponding Gibbs free energies. (b) B-C-O fragments involved in lowest energy CO dimerization at B_2 (top) and B_3 (bottom) sites and their respective change in $-\mathrm{ICOHP}_{E_F}$ values upon dimerization.

Conclusion

In summary, we have presented a realistic model of a surface copper boride under operational electrochemical conditions, followed by mechanistic studies of eCORR that indicate C_2 selectivity of this electrocatalyst. Excess B hydrogenation was found to cause B chain breaking, and surface degradation under cathodic potentials. However, this process is kinetically inhibited by HER under operational conditions, resulting in a kinetically metastable H-covered copper boride surface. A potential-dependent grand canonical ensemble for the

metastable configurations of the H-covered catalyst surface was constructed using GCGA global optimization and GCDFT calculations. Two configurations of the catalyst, namely, LC (-0.6 V_{SHE}) and HC (-0.8 V_{SHE}) were identified to dominate this ensemble, with the formation of the latter again appearing to be kinetically hindered. Investigation of C_1 and C_2 pathways for eCORR on these configurations revealed site-dependent reactivity with B sites significantly outperforming Cu sites in CO binding and electroreduction. The LC (-0.6 V_{SHE}) configuration is C_2-selective at electrode potentials under -0.6 V_{SHE}, facilitating the C–C coupling (via *CO dimerization) over CO hydrogenation (via *CHO formation). In contrast, the HC (-0.8 V_{SHE}) is C_1-selective under all relevant potentials. Thus, the metastability of the LC (-0.6 V_{SHE}) state of the catalyst endows it with high C_2 selectivity at electrode potentials below -0.6 V_{SHE}. This C_2 selectivity is primarily attributed to neighboring B sites in B_{3+} chains rather than neighboring B sites in B_2 chains, as supported by chemical bonding analysis. Overall, this work highlights the unusual and very important B-centered reactivity on the surface copper boride, demonstrating the potential of leveraging B-centered reactivity on transition metal boride surfaces to drive electrocatalytic processes, including the challenging reduction of $CO_{(2)}$ to C_2 products.[43,44]

Computational Methods

Model Setup

We constructed the unit cell with cell dimension of $21.84\,\text{Å} \times 15.96\,\text{Å}$ with $\alpha = 70.28°$ (as reported experimentally[23]) consisting of a 4×1 supercell of surface copper boride on a 3-layer $\sqrt{73} \times \sqrt{39}$ superstructure of Cu(111), corresponding to a repeating $Cu_{32}B_{56}$ surface. The bottom layer of the slab was constrained as the bulk region with everything else allowed to relax. A vacuum of $20\,\text{Å}$ was added in the z-direction to avoid interaction between periodic images.

DFT Calculations

The local optimizations and energy calculation are performed with the RPBE functional[45] and corresponding pseudopotentials in the projector-augmented wave (PAW)[46] scheme using the VASP program (version 5.4.4).[47–50] The convergence criteria for electronic and force minimization were set to 10^{-5} eV and 0.10 eV/Å during the global optimization and 10^{-6} eV and 0.03 eV/Å for the final refinement. Due to the relatively large system and sampling size, only the Γ *k*-point was sampled in the reciprocal space of the Brillouin zone throughout, and the cutoff energy for the kinetic energy of the plane-waves was 400 eV. The vibrational contributions to the free energy by the slab atoms are neglected considering their small contribution and high computational cost.[51] The zero-point energy (ZPE) and thermal contribution terms of the adsorbates are obtained from frequency calculations and evaluated at 298.15 K, with the partial pressure of gaseous species (H_2 and CO) being set to 1 atm (see Supporting Information, Section S7).

The transition states (TS) were located using climbing image nudged elastic band (CI-NEB) method[52] and each TS geometry was confirmed to have only one imaginary mode. The resulting barrier was refined using GCDFT calculations and accordingly, energies were reported at constant potential(s).

Bader charges were calculated using the Bader Charge Analysis program.[53] COHP analysis is performed using the LOBSTER program.[42] Quantum theory of atoms in molecules analysis

is performed using the critic2 program.[54] Isosurfaces are visualized using the VESTA program.[55]

Grand Canonical Genetic Algorithm

The chemical space of CuB surface reconstruction and H coverage was sampled by grand canonical genetic algorithm (GCGA) global optimization using our open-source GOCIA python package.[29] The system is treated as a grand canonical ensemble of H adsorbates, and the search target is to minimize the coverage-dependent grand canonical free energy Ω_{ads}:

$$\Omega_{\mathrm{ads}} = U - TS - \mu_{\mathrm{H}} N_{\mathrm{H}} \approx E^{\mathrm{slab}-n_{\mathrm{H}}} - E^{\mathrm{slab}} - n_{\mathrm{H}}\mu_{\mathrm{H}}$$

where $E^{\mathrm{slab}-n_{\mathrm{H}}}$ and E^{slab} are electronic energies of the adsorbate-covered and the bare CuB surface, respectively. The vibrational contributions to the free energy by the slab atoms are neglected considering their small contribution and high computational cost.[51] The chemical potential of H, μ_{H} was calculated as:

$$\mu_{\mathrm{H}}(\mathrm{pH}, U, T) = \frac{1}{2}E_{\mathrm{H_2}}^{\mathrm{gas}} - \ln(10)\, k_{\mathrm{B}} T \mathrm{pH} - |e| U_{\mathrm{SHE}} + \left(\mathrm{ZPE}^{\mathrm{gas}} + C_p^{\mathrm{gas}} - \mathrm{TS}^{\mathrm{gas}}\right) - (\mathrm{ZPE}^{\mathrm{ads}} + C_p^{\mathrm{ads}} - TS^{\mathrm{ads}})$$

where the pH and *U* (in SHE scale)-dependent terms are calculated using the computational hydrogen electrode model. The ZPE and thermal contribution terms of the adsorbates are obtained from frequency calculations and evaluated at 298.15 K.

A population size of 25 and a mutation rate of 40% were used for the GCGA sampling. The pool of initial candidates is generated using the box sampling method in GOCIA, which places adsorbates with random positions and orientations into the sampling box. The surface Cu and B surface atoms are perturbed in the initial generation, and their arrangements are allowed to relax as we sample different H coverages and configurations. Any other surface B configurations other than chains turn out to be thermodynamically unfavorable in the mid to low H coverage regime.

Grand Canonical DFT Calculations

Under constant electrochemical potential, the electrode surface represents a grand canonical ensemble of electrons where the number of electrons is varied to adapt to the change in the work function of the surface. The potential-dependent electronic grand canonical free energy of the surface Ω_{el} was approximated by a surface charging model[56]

$$\Omega_{\mathrm{el}}(U) = E(U) - q(U)FU \approx E(U_0) - \frac{1}{2}C(U - U_0)^2$$

which treats the electrochemical interface as an effective capacitor. Here, $E(U)$ is the electronic energy of the surface under a potential U that is calculated by refencing the Fermi level of the system against the vacuum level. $q(U)$ is the surface charge difference referenced against the neutral system and F is the Faraday constant. U_0 stands for the potential of zero charge in vacuum scale and C is the effective capacitance.

The self-consistent implicit solvation model VASPsol[57] is used to represent the polarizable electrolyte region. The surface slab is symmetrized via a point center symmetry operation to avoid an asymmetric potential in the implicit solvation region. The thickness of the implicit solvent slab is increased to 5λ, where λ (the Debye screening length) is evaluated by[58]

$$\lambda \approx \frac{3}{\sqrt{I}}\text{Å}$$

where *I* is the ionic strength in M; in this study, we take it to be 0.1 to model the 0.1 M KCl electrolyte used by Sargent et al.[21] Hence, the implicit solvent thickness is set to 50 Å for the symmetrized slab.

By varying the number of electrons in the system, $E(U)$ of the system at the corresponding U and $q(U)$ can be obtained, and thereby, a quadratic relation between $\Omega_{\mathrm{el}}(U)$ and U can be fitted by sampling a series of q values. Multiple calculations were performed at extra charges of -3, -2, -1, 0, +1, +2 |e| per simulation box to fit the quadratic potential-dependent free energy relation. The U (in vacuum scale) can be converted into the SHE scale by referencing it against the benchmarked value (4.60 V for VASPsol).[59]

The final coverage- and potential-dependent grand canonical free energy Ω_{tot} was approximated by:

$$\Omega_{\mathrm{tot}}(n_{\mathrm{H}}, U) = \Omega_{\mathrm{ads}}^{\mathrm{slab}-n_{\mathrm{H}}}(U) - \Omega_{\mathrm{ads}}^{\mathrm{slab}}(U) - n_{\mathrm{H}}\mu_{\mathrm{H}}(\mathrm{pH}, U, T)$$

Given the considerable computational cost involved, the GCDFT calculations were performed not during the GCGA sampling but on a subset of structures (within 0.2 eV from the GM of each coverage state in the metastable plateau) from the final ensemble, *a posteriori*. This approach greatly reduced the computational expense of constructing the potential-dependent grand canonical ensemble while capturing the energetics of key accessible states in the ensemble.

Data Availability

Database of all optimized structures used in this study is available at the following public repository: https://doi.org/10.5281/zenodo.17478545.

Supporting Information

Plots of GCGA sampling and GCDFT-derived potential-dependent ensembles; kinetics of B-chain breaking; AIMD simulations; charge and bonding analysis of hydrogenated CuB surfaces; Cu/B-CO bonding analysis; thermal corrections; and structures of reaction intermediates.

Acknowledgements

This work was supported as part of the Center for Closing the Carbon Cycle, an Energy Frontier Research Center funded by the U.S. Department of Energy, Office of Science, Basic Energy Sciences under Award Number DE-SC0023427. Z. Z. was supported previously by the Dissertation Year Award at UCLA and currently by the Stanford Energy Fellowship at the Stanford Precourt Institute for Energy. Our calculations utilized resources of Perlmutter of the National Energy Research Scientific Computing Center (NERSC) under Contract DE-AC02-05CH11231. We thank Dr. Yulan Han for helpful discussions.

References

(1) Seh, Z. W.; Kibsgaard, J.; Dickens, C. F.; Chorkendorff, I.; Nørskov, J. K.; Jaramillo, T. F. Combining Theory and Experiment in Electrocatalysis: Insights into Materials Design. *Science* **2017**, *355* (6321), eaad4998. https://doi.org/10.1126/science.aad4998.

(2) Birdja, Y. Y.; Pérez-Gallent, E.; Figueiredo, M. C.; Göttle, A. J.; Calle-Vallejo, F.; Koper, M. T. M. Advances and Challenges in Understanding the Electrocatalytic Conversion of Carbon Dioxide to Fuels. *Nat. Energy.* **2019**, *4* (9), 732–745. https://doi.org/10.1038/s41560-019-0450-y.

(3) Gao, D.; Arán-Ais, R. M.; Jeon, H. S.; Roldan Cuenya, B. Rational Catalyst and Electrolyte Design for CO2 Electroreduction towards Multicarbon Products. *Nat. Catal.* **2019**, *2* (3), 198–210. https://doi.org/10.1038/s41929-019-0235-5.

(4) Cabana, J.; Alaan, T.; Crabtree, G. W.; Hatzell, M. C.; Manthiram, K.; Steingart, D. A.; Zenyuk, I.; Jiao, F.; Vojvodic, A.; Yang, J. Y.; Balsara, N. P.; Persson, K. A.; Siegel, D. J.; Haynes, C. L.; Mauzeroll, J.; Shen, M.; Venton, B. J.; Balke, N.; Rodríguez-López, J.; Rolison, D. R.; Shahbazian-Yassar, R.; Srinivasan, V.; Chaudhuri, S.; Couet, A.; Hattrick-Simpers, J. NGenE 2021: Electrochemistry Is Everywhere. *ACS Energy Lett.* **2022**, *7* (1), 368–374. https://doi.org/10.1021/acsenergylett.1c02608.

(5) Wang, L.; Nitopi, S. A.; Bertheussen, E.; Orazov, M.; Morales-Guio, C. G.; Liu, X.; Higgins, D. C.; Chan, K.; Nørskov, J. K.; Hahn, C.; Jaramillo, T. F. Electrochemical Carbon Monoxide Reduction on Polycrystalline Copper: Effects of Potential, Pressure, and pH on Selectivity toward Multicarbon and Oxygenated Products. *ACS Catal.* **2018**, *8* (8), 7445–7454. https://doi.org/10.1021/acscatal.8b01200.

(6) Zhang, G.; Zhao, Z.-J.; Cheng, D.; Li, H.; Yu, J.; Wang, Q.; Gao, H.; Guo, J.; Wang, H.; Ozin, G. A.; Wang, T.; Gong, J. Efficient CO2 Electroreduction on Facet-Selective Copper Films with High Conversion Rate. *Nat. Commun.* **2021**, *12* (1), 5745. https://doi.org/10.1038/s41467-021-26053-w.

(7) Nitopi, S.; Bertheussen, E.; Scott, S. B.; Liu, X.; Engstfeld, A. K.; Horch, S.; Seger, B.; Stephens, I. E. L.; Chan, K.; Hahn, C.; Nørskov, J. K.; Jaramillo, T. F.; Chorkendorff, I. Progress and Perspectives of Electrochemical CO_2 Reduction on Copper in Aqueous Electrolyte. *Chem. Rev.* **2019**, *119* (12), 7610–7672. https://doi.org/10.1021/acs.chemrev.8b00705.

(8) Dattila, F.; Seemakurthi, R. R.; Zhou, Y.; López, N. Modeling Operando Electrochemical CO2 Reduction. *Chem. Rev.* **2022**, *122* (12), 11085–11130. https://doi.org/10.1021/acs.chemrev.1c00690.

(9) Li, J.; Ozden, A.; Wan, M.; Hu, Y.; Li, F.; Wang, Y.; Zamani, R. R.; Ren, D.; Wang, Z.; Xu, Y.; Nam, D.-H.; Wicks, J.; Chen, B.; Wang, X.; Luo, M.; Graetzel, M.; Che, F.; Sargent, E. H.; Sinton, D. Silica-Copper Catalyst Interfaces Enable Carbon-Carbon Coupling towards Ethylene Electrosynthesis. *Nat. Commun.* **2021**, *12* (1), 2808. https://doi.org/10.1038/s41467-021-23023-0.

(10) Xu, A.; Hung, S.-F.; Cao, A.; Wang, Z.; Karmodak, N.; Huang, J. E.; Yan, Y.; Sedighian Rasouli, A.; Ozden, A.; Wu, F.-Y.; Lin, Z.-Y.; Tsai, H.-J.; Lee, T.-J.; Li, F.; Luo, M.; Wang, Y.; Wang, X.; Abed, J.; Wang, Z.; Nam, D.-H.; Li, Y. C.; Ip, A. H.; Sinton, D.; Dong, C.; Sargent, E. H.

Copper/Alkaline Earth Metal Oxide Interfaces for Electrochemical CO2-to-Alcohol Conversion by Selective Hydrogenation. *Nat. Catal.* **2022**, *5* (12), 1081–1088. https://doi.org/10.1038/s41929-022-00880-6.

(11) Li, F.; Thevenon, A.; Rosas-Hernández, A.; Wang, Z.; Li, Y.; Gabardo, C. M.; Ozden, A.; Dinh, C. T.; Li, J.; Wang, Y.; Edwards, J. P.; Xu, Y.; McCallum, C.; Tao, L.; Liang, Z.-Q.; Luo, M.; Wang, X.; Li, H.; O'Brien, C. P.; Tan, C.-S.; Nam, D.-H.; Quintero-Bermudez, R.; Zhuang, T.-T.; Li, Y. C.; Han, Z.; Britt, R. D.; Sinton, D.; Agapie, T.; Peters, J. C.; Sargent, E. H. Molecular Tuning of CO2-to-Ethylene Conversion. *Nature* **2020**, *577* (7791), 509–513. https://doi.org/10.1038/s41586-019-1782-2.

(12) Li, J.; Li, F.; Liu, C.; Wei, F.; Gong, J.; Li, W.; Xue, L.; Yin, J.; Xiao, L.; Wang, G.; Lu, J.; Zhuang, L. Polyquinone Modification Promotes CO2 Activation and Conversion to C2+ Products over Copper Electrode. *ACS Energy Lett.* **2022**, *7* (11), 4045–4051. https://doi.org/10.1021/acsenergylett.2c01955.

(13) Xiao, H.; Goddard, W. A.; Cheng, T.; Liu, Y. Cu Metal Embedded in Oxidized Matrix Catalyst to Promote CO_2 Activation and CO Dimerization for Electrochemical Reduction of CO_2. *Proc. Natl. Acad. Sci. U.S.A.* **2017**, *114* (26), 6685–6688. https://doi.org/10.1073/pnas.1702405114.

(14) De Luna, P.; Quintero-Bermudez, R.; Dinh, C.-T.; Ross, M. B.; Bushuyev, O. S.; Todorović, P.; Regier, T.; Kelley, S. O.; Yang, P.; Sargent, E. H. Catalyst Electro-Redeposition Controls Morphology and Oxidation State for Selective Carbon Dioxide Reduction. *Nat. Catal.* **2018**, *1* (2), 103–110. https://doi.org/10.1038/s41929-017-0018-9.

(15) Ren, D.; Deng, Y.; Handoko, A. D.; Chen, C. S.; Malkhandi, S.; Yeo, B. S. Selective Electrochemical Reduction of Carbon Dioxide to Ethylene and Ethanol on Copper(I) Oxide Catalysts. *ACS Catal.* **2015**, *5* (5), 2814–2821. https://doi.org/10.1021/cs502128q.

(16) Larrazábal, G. O.; Martín, A. J.; Krumeich, F.; Hauert, R.; Pérez-Ramírez, J. Solvothermally-Prepared Cu_2 O Electrocatalysts for CO_2 Reduction with Tunable Selectivity by the Introduction of p-Block Elements. *ChemSusChem* **2017**, *10* (6), 1255–1265. https://doi.org/10.1002/cssc.201601578.

(17) Lee, S.; Kim, D.; Lee, J. Electrocatalytic Production of C3-C4 Compounds by Conversion of CO2 on a Chloride-Induced Bi-Phasic Cu2O-Cu Catalyst. *Angew. Chem. Int. Ed.* **2015**, *54* (49), 14701–14705. https://doi.org/10.1002/anie.201505730.

(18) Favaro, M.; Xiao, H.; Cheng, T.; Goddard, W. A.; Yano, J.; Crumlin, E. J. Subsurface Oxide Plays a Critical Role in CO2 Activation by Cu(111) Surfaces to Form Chemisorbed CO2, the First Step in Reduction of CO2. *Proceedings of the National Academy of Sciences* **2017**, *114* (26), 6706–6711. https://doi.org/10.1073/pnas.1701405114.

(19) Li, M.; Ma, Y.; Chen, J.; Lawrence, R.; Luo, W.; Sacchi, M.; Jiang, W.; Yang, J. Residual Chlorine Induced Cationic Active Species on a Porous Copper Electrocatalyst for Highly Stable Electrochemical CO2 Reduction to C2+. *Angew. Chem. Int. Ed.* **2021**, *60* (20), 11487–11493. https://doi.org/10.1002/anie.202102606.

(20) Lim, H.-K.; Shin, H.; Goddard, W. A. I.; Hwang, Y. J.; Min, B. K.; Kim, H. Embedding Covalency into Metal Catalysts for Efficient Electrochemical Conversion of CO2. *J. Am. Chem. Soc.* **2014**, *136* (32), 11355–11361. https://doi.org/10.1021/ja503782w.

(21) Zhou, Y.; Che, F.; Liu, M.; Zou, C.; Liang, Z.; De Luna, P.; Yuan, H.; Li, J.; Wang, Z.; Xie, H.; Li, H.; Chen, P.; Bladt, E.; Quintero-Bermudez, R.; Sham, T.-K.; Bals, S.; Hofkens, J.; Sinton, D.; Chen, G.; Sargent, E. H. Dopant-Induced Electron Localization Drives CO2 Reduction to C2 Hydrocarbons. *Nature Chem.* **2018**, *10* (9), 974–980. https://doi.org/10.1038/s41557-018-0092-x.

(22) Wang, S.; Wang, L.; Zhu, X.; Zhuang, Y.; Niu, X.; Zhao, Q. A Covalency-Aided Electrochemical Mechanism for CO_2 Reduction: The Synergistic Effect of Copper and Boron Dual Active Sites Drives the Formation of a High-Efficiency Ethanol Product. *Nanoscale* **2023**, *15* (44), 17776–17784. https://doi.org/10.1039/D3NR04288J.

(23) Yue, C.; Weng, X.-J.; Gao, G.; Oganov, A. R.; Dong, X.; Shao, X.; Wang, X.; Sun, J.; Xu, B.; Wang, H.-T.; Zhou, X.-F.; Tian, Y. Formation of Copper Boride on Cu(111). *Fundamental Research* **2021**, *1* (4), 482–487. https://doi.org/10.1016/j.fmre.2021.05.003.

(24) Weng, X.-J.; Bai, J.; Hou, J.; Zhu, Y.; Wang, L.; Li, P.; Nie, A.; Xu, B.; Zhou, X.-F.; Tian, Y. Experimental Evidence of Surface Copper Boride. *Nano Res.* **2023**, *16* (7), 9602–9607. https://doi.org/10.1007/s12274-023-5496-2.

(25) Tsujikawa, Y.; Zhang, X.; Horio, M.; Komori, F.; Nakashima, T.; Ando, Y.; Kondo, T.; Matsuda, I. Structure and Electronic State of Boron Atomic Chains on a Noble Metal (111) Surface. *e-J. Surf. Sci. Nanotechnol.* **2023**, *22* (1), 1–8. https://doi.org/10.1380/ejssnt.2023-058.

(26) Zhang, Z.; Wei, Z.; Sautet, P.; Alexandrova, A. N. Hydrogen-Induced Restructuring of a Cu(100) Electrode in Electroreduction Conditions. *J. Am. Chem. Soc.* **2022**, *144* (42), 19284–19293. https://doi.org/10.1021/jacs.2c06188.

(27) Cheng, D.; Wei, Z.; Zhang, Z.; Broekmann, P.; Alexandrova, A. N.; Sautet, P. Restructuring and Activation of Cu(111) under Electrocatalytic Reduction Conditions. *Angewandte Chemie* **2023**, *135* (20), e202218575. https://doi.org/10.1002/ange.202218575.

(28) Zhang, Z.; Gee, W.; Sautet, P.; Alexandrova, A. N. H and CO Co-Induced Roughening of Cu Surface in CO_2 Electroreduction Conditions. *J. Am. Chem. Soc.* **2024**, *146* (23), 16119–16127. https://doi.org/10.1021/jacs.4c03515.

(29) Zhang, Z.; Gee, W.; Lavroff, R. H.; Alexandrova, A. N. GOCIA: A Grand Canonical Global Optimizer for Clusters, Interfaces, and Adsorbates. *Phys. Chem. Chem. Phys.* **2025**, *27* (2), 696–706. https://doi.org/10.1039/D4CP03801K.

(30) Bader, R. F. W. *Atoms in Molecules: A Quantum Theory*; Oxford University PressOxford, 1990. https://doi.org/10.1093/oso/9780198551683.001.0001.

(31) Bader, R. F. W. A Quantum Theory of Molecular Structure and Its Applications. *Chem. Rev.* **1991**, *91* (5), 893–928. https://doi.org/10.1021/cr00005a013.

(32) Poths, P.; Vargas, S.; Sautet, P.; Alexandrova, A. N. Thermodynamic Equilibrium versus Kinetic Trapping: Thermalization of Cluster Catalyst Ensembles Can Extend Beyond Reaction Time Scales. *ACS Catal.* **2024**, *14* (7), 5403–5415. https://doi.org/10.1021/acscatal.3c06154.

(33) Zhang, Z.; Abild-Pedersen, F. Off-Equilibrium Reactivity of Boron-Enriched Metal Diboride Surfaces in Electroreduction Conditions. *ACS Catal.* **2025**, *15* (14), 12340–12350. https://doi.org/10.1021/acscatal.5c04054.

(34) Kelly, S. R.; Heenen, H. H.; Govindarajan, N.; Chan, K.; Nørskov, J. K. OH Binding Energy as a Universal Descriptor of the Potential of Zero Charge on Transition Metal Surfaces. *J. Phys. Chem. C* **2022**, *126* (12), 5521–5528. https://doi.org/10.1021/acs.jpcc.1c10362.

(35) Sebastián-Pascual, P.; Sarabia, F. J.; Climent, V.; Feliu, J. M.; Escudero-Escribano, M. Elucidating the Structure of the Cu-Alkaline Electrochemical Interface with the Laser-Induced Temperature Jump Method. *J. Phys. Chem. C* **2020**, *124* (42), 23253–23259. https://doi.org/10.1021/acs.jpcc.0c07821.

(36) Łukomska, A.; Sobkowski, J. Potential of Zero Charge of Monocrystalline Copper Electrodes in Perchlorate Solutions. *Journal of Electroanalytical Chemistry* **2004**, *567* (1), 95–102. https://doi.org/10.1016/j.jelechem.2003.11.063.

(37) Montoya, J. H.; Shi, C.; Chan, K.; Nørskov, J. K. Theoretical Insights into a CO Dimerization Mechanism in CO_2 Electroreduction. *J. Phys. Chem. Lett.* **2015**, *6* (11), 2032–2037. https://doi.org/10.1021/acs.jpclett.5b00722.

(38) Xiao, H.; Cheng, T.; Goddard, W. A.; Sundararaman, R. Mechanistic Explanation of the pH Dependence and Onset Potentials for Hydrocarbon Products from Electrochemical Reduction of CO on Cu (111). *J. Am. Chem. Soc.* **2016**, *138* (2), 483–486. https://doi.org/10.1021/jacs.5b11390.

(39) Cheng, T.; Xiao, H.; Goddard, W. A. Full Atomistic Reaction Mechanism with Kinetics for CO Reduction on Cu(100) from Ab Initio Molecular Dynamics Free-Energy Calculations at 298 K. *Proc. Natl. Acad. Sci. U.S.A.* **2017**, *114* (8), 1795–1800. https://doi.org/10.1073/pnas.1612106114.

(40) Garza, A. J.; Bell, A. T.; Head-Gordon, M. Mechanism of CO_2 Reduction at Copper Surfaces: Pathways to C_2 Products. *ACS Catal.* **2018**, *8* (2), 1490–1499. https://doi.org/10.1021/acscatal.7b03477.

(41) Todorova, T. K.; Schreiber, M. W.; Fontecave, M. Mechanistic Understanding of CO_2 Reduction Reaction (CO2RR) Toward Multicarbon Products by Heterogeneous Copper-Based Catalysts. *ACS Catal.* **2020**, *10* (3), 1754–1768. https://doi.org/10.1021/acscatal.9b04746.

(42) Nelson, R.; Ertural, C.; George, J.; Deringer, V. L.; Hautier, G.; Dronskowski, R. LOBSTER : Local Orbital Projections, Atomic Charges, and Chemical-bonding Analysis from PROJECTOR-AUGMENTED-WAVE-BASED Density-functional Theory. *J Comput Chem* **2020**, *41* (21), 1931–1940. https://doi.org/10.1002/jcc.26353.

(43) Zhu, C.; Wen, C.; Wang, M.; Zhang, M.; Geng, Y.; Su, Z. Non-Metal Boron Atoms on a CuB_{12} Monolayer as Efficient Catalytic Sites for Urea Production. *Chem. Sci.* **2022**, *13* (5), 1342–1354. https://doi.org/10.1039/D1SC04845G.

(44) Liu, M.; Balamurugan, J.; Liang, T.; Liu, C. Theoretical Study of B12 Borophene Supported Metal for Electrocatalytic CO2 Reduction Reaction. *Applied Surface Science* **2024**, *642*, 158594. https://doi.org/10.1016/j.apsusc.2023.158594.

(45) Hammer, B.; Hansen, L. B.; Nørskov, J. K. Improved Adsorption Energetics within Density-Functional Theory Using Revised Perdew-Burke-Ernzerhof Functionals. *Phys. Rev. B* **1999**, *59* (11), 7413–7421. https://doi.org/10.1103/PhysRevB.59.7413.

(46) Kresse, G.; Joubert, D. From Ultrasoft Pseudopotentials to the Projector Augmented-Wave Method. *Phys. Rev. B* **1999**, *59* (3), 1758–1775. https://doi.org/10.1103/PhysRevB.59.1758.

(47) Kresse, G.; Furthmüller, J. Efficiency of Ab-Initio Total Energy Calculations for Metals and Semiconductors Using a Plane-Wave Basis Set. *Computational Materials Science* **1996**, *6* (1), 15–50. https://doi.org/10.1016/0927-0256(96)00008-0.

(48) Kresse, G.; Furthmüller, J. Efficient Iterative Schemes for *Ab Initio* Total-Energy Calculations Using a Plane-Wave Basis Set. *Phys. Rev. B* **1996**, *54* (16), 11169–11186. https://doi.org/10.1103/PhysRevB.54.11169.

(49) Kresse, G. Ab Initio Molecular Dynamics for Liquid Metals. *Journal of Non-Crystalline Solids* **1995**, *192–193*, 222–229. https://doi.org/10.1016/0022-3093(95)00355-X.

(50) Kresse, G.; Hafner, J. *Ab Initio* Molecular-Dynamics Simulation of the Liquid-Metal–Amorphous-Semiconductor Transition in Germanium. *Phys. Rev. B* **1994**, *49* (20), 14251–14269. https://doi.org/10.1103/PhysRevB.49.14251.

(51) Sun, G.; Alexandrova, A. N.; Sautet, P. Structural Rearrangements of Subnanometer Cu Oxide Clusters Govern Catalytic Oxidation. *ACS Catal.* **2020**, *10* (9), 5309–5317. https://doi.org/10.1021/acscatal.0c00824.

(52) Henkelman, G.; Uberuaga, B. P.; Jónsson, H. A Climbing Image Nudged Elastic Band Method for Finding Saddle Points and Minimum Energy Paths. *The Journal of Chemical Physics* **2000**, *113* (22), 9901–9904. https://doi.org/10.1063/1.1329672.

(53) Yu, M.; Trinkle, D. R. Accurate and Efficient Algorithm for Bader Charge Integration. *The Journal of Chemical Physics* **2011**, *134* (6), 064111. https://doi.org/10.1063/1.3553716.

(54) Otero-de-la-Roza, A.; Johnson, E. R.; Luaña, V. Critic2: A Program for Real-Space Analysis of Quantum Chemical Interactions in Solids. *Computer Physics Communications* **2014**, *185* (3), 1007–1018. https://doi.org/10.1016/j.cpc.2013.10.026.

(55) Momma, K.; Izumi, F. *VESTA 3* for Three-Dimensional Visualization of Crystal, Volumetric and Morphology Data. *J Appl Crystallogr* **2011**, *44* (6), 1272–1276. https://doi.org/10.1107/S0021889811038970.

(56) Steinmann, S. N.; Michel, C.; Schwiedernoch, R.; Sautet, P. Impacts of Electrode Potentials and Solvents on the Electroreduction of CO_2: A Comparison of Theoretical Approaches. *Phys. Chem. Chem. Phys.* **2015**, *17* (21), 13949–13963. https://doi.org/10.1039/C5CP00946D.

(57) Mathew, K.; Sundararaman, R.; Letchworth-Weaver, K.; Arias, T. A.; Hennig, R. G. Implicit Solvation Model for Density-Functional Study of Nanocrystal Surfaces and Reaction Pathways. *The Journal of Chemical Physics* **2014**, *140* (8), 084106. https://doi.org/10.1063/1.4865107.

(58) Steinmann, S. N.; Sautet, P. Assessing a First-Principles Model of an Electrochemical Interface by Comparison with Experiment. *J. Phys. Chem. C* **2016**, *120* (10), 5619–5623. https://doi.org/10.1021/acs.jpcc.6b01938.

(59) Mathew, K.; Kolluru, V. S. C.; Mula, S.; Steinmann, S. N.; Hennig, R. G. Implicit Self-Consistent Electrolyte Model in Plane-Wave Density-Functional Theory. *The Journal of Chemical Physics* **2019**, *151* (23), 234101. https://doi.org/10.1063/1.5132354.

TOC Graphic